Recapitulation of folliculogenesis to ovulation in a biomimetic micro-cavity ovary

Min Ye
Tsinghua University https://orcid.org/0000-0003-1065-0034
Yiran Shan
Tsinghua University
Bingchuan Lu
Tsinghua University
Hao Luo
Tsinghua University
Zixuan Wang
Tsinghua University
Yuzhi Guo
Tsinghua University
Liliang Ouyang
Tsinghua University https://orcid.org/0000-0003-4177-8698
Jin Gu
Tsinghua University https://orcid.org/0000-0003-3968-8036
Zhuo Xiong
Tsinghua University
Ting Zhang (t-zhang@mail.tsinghua.edu.cn)
Tsinghua University

Article

Keywords:

Posted Date: July 8th, 2022

DOI: https://doi.org/10.21203/rs.3.rs-1807077/v1

Recapitulation of folliculogenesis to ovulation in a biomimetic micro-cavity ovary

Min Ye[1, 2, 3], Yiran Shan[4], Bingchuan Lu[1, 2, 3], Hao Luo[1, 2, 3], Zixuan Wang[1, 2, 3], Yuzhi Guo[1, 2, 3], Liliang Ouyang[1, 2, 3], Jin Gu[4], Zhuo Xiong[1, 2, 3, *], Ting Zhang[1, 2, 3, *]

1. Biomanufacturing Center, Department of Mechanical Engineering, Tsinghua University, Beijing, 100084, China.
2. Biomanufacturing and Rapid Forming Technology Key Laboratory of Beijing, Beijing, 100084, China.
3. "Biomanufacturing and Engineering Living Systems" Innovation International Talents Base (111 Base), Beijing, 100084, China
4. MOE Key Laboratory of Bioinformatics, BNRIST Bioinformatics Division, Department of Automation, Tsinghua University, Beijing, 100084, China.

* Corresponding authors

Email: Ting Zhang, t-zhang@mail.tsinghua.edu.cn

Zhuo Xiong, xiongzhuo@tsinghua.edu.cn

Abstract

Ovary disease is a major cause of female infertility and could disrupt the hormone balance, which may cause multi-organ disorders in the long-term effect. However, conventional artificial ovary techniques usually encapsulate follicles in 3D hydrogels and block the ovulation ability. In this study, we fabricated a biomimetic micro-cavity ovary by a microsphere-templated technique to recapitulate the ovulation process, where sacrificial gelatin microspheres were mixed with photo-crosslinkable gelatin methacryloyl (GelMA) to engineer an open cavity niche for follicle growth. The microcavity's parameters were optimized to be suitable for follicle growth. With that, we showed that the micro-cavity ovary could support the follicle growth to antral stage and the ovulation of meiosis-matured oocytes out of the micro-cavity ovary without extra manipulation. The ovulated oocyte was characterized in a great quality. This technique would be of great advantage to be further applied in clinics that recover natural conception after *in vivo* transplantation of the biomimetic ovary.

Introduction

The artificial ovary has been developed for decades to replace the diseased organ caused by polycystic ovarian syndrome (PCOS) or be disrupted by chemotherapy and radiotherapy. The requirement of a functional artificial ovary includes supporting follicle maturation, recovering hormone levels, and ultimately restoring ovulation. Although assisted reproductive technologies (ARTs) can assist patients in getting

pregnant, ARTs do not meet the increasing clinical demands such as long-term hormone restoration or recovery of natural conception. Usually, the artificial ovary consists of germ cells that are implanted or encapsulated in biomaterials. Conventional culture methods use hydrogel to encapsulate premature follicles that supply a 3D environment for follicle growth and maturation. Natural hydrogel, semi-natural hydrogel, or synthetic hydrogels, including Matrigel[1-3], collagen [4], Calcium alginate matrix[2,3,5,6], Hyaluronan[7], Polyethylene glycol (PEG)[8] can be chosen as candidates for fabricating the artificial ovary. However, these culturing methods did not restore the ovulation ability since the rupture of oocytes was blocked by the enclosed hydrogel.

Ovulation is defined as the ovary releasing mature oocytes into fallopian tubes, waiting for fertilization. After puberty, immature follicles respond to gonadotropic hormone (FSH/LH) levels[9,10] begin to increase the follicle size, and develop a cavity filled with follicular fluid. The process was also known as folliculogenesis. At the late stage of folliculogenesis, the oocyte resumes from meiosis arrest resulting in the extrusion of the first polar body and arrests again at the meiotic metaphase II stage (MII). Meanwhile, the MII oocyte is ruptured out of the ovary stimulated by the LH surge[9,11-13]. Besides of the growth factor signal, the mechanical signaling or mechanotransduction plays an essential role throughout the dynamic lifespan of the ovarian follicle including oocyte growth, meiotic maturation, and ultimately ovulation[14]. An *in vitro* follicle 3D culturing study used alginate-fibrin network hydrogel to mimic the ovarian rigidity, giving a hint that the maturation ratio of oocytes would be enhanced by mimicking the ovarian mechanical enviroment[15]. Furthermore, we noticed that many matured follicles grow near the surface of ovaries[16,17] . Apparently, this physiological structure assists the ovary to release MII oocytes directly into fallopian tubes. Since the ovulation process is a combination of coordinated cellular processes, it emerges as one of the challenging problems to be recapitulated in an artificial ovary.

To build a biomimetic organ, a micro-mold approach was applied. The mold approach was widely used in 3D tissue construction[18-22] due to its precise control of the mold shape and size. However, the molding approach alone has little effort in building internal structures of tissues. To build a sophisticated tissue, microfluidic technology is integrated with the molding approach to increase the complexity and geometry of the fabricated structure, for example, by providing microcavities. Microfluidic technology was defined as producing and manipulating fluids in a small volume of particles as limited as 10^{18} liters[23,24]. In recent perspectives, living organisms are built followed a bottom-up fashion since all lives start based on cellular behaviors such as cell proliferation, migration, and differentiation. The microfluidic technology was of great advantage in fabricating at the bottom-up level, for it can manipulate the microparticles even at a single-cell level[25,26].

In this study, we assumed that mimicking the pattern of follicles growing near the surface of the ovary might assist in retaining the ovulation ability in a bio-engineered ovary. Herein, we manipulated the microsphere to fabricate a biomimetic micro-cavity

ovary using a microfluidic and mold approach. We used gelatin methacryloyl (GelMA), a biocompatible hydrogel widely used to fabricate artificial organs[27-30], to construct the micro-cavity structure. To mimic the ovarian mechanical environment, we first investigated the effects of GelMA properties and cavity size on follicle growth, and optimized the concentration of GelMA to 10%, the substitution of methacryloyl to 90%, and the cavity size to 600 μm. As a result, we successfully recorded that the oocyte was ovulated out of the micro-cavity ovary and confirmed that the ovulated oocyte was of good quality and fertilized. We also investigate the mechanoresponsive gene *Yap1* was 1.2-fold increase in the micro-cavity ovulated oocyte, indicating multiple mechanical cues should be considered to optimize the micro-cavity ovary. By applying the new technology, we solved the challenging obstacle of ovulation in the field of artificial ovary construction, and our model was promising for future clinic transplantation.

Results

Bio-fabrication of the micro-cavity ovary and characterization

The strategy of fabricating and characterizing the micro-cavity ovary is shown in Figure 1. GelMA is synthesized through the reaction of gelatin with methacrylic anhydride (MA). The percentage of replaced amino groups on the side chains of gelatin and the concentration of GelMA affected the stiffness, then ultimately affected the follicle quality. Therefore, the replaced percentage and the concentration of GelMA should be determined before the final fabrication (Fig. 1a). Then the microfluidic was employed to produce gelatin microspheres for casting the surface morphology of GelMA to create microcavities. The size of the microsphere was also waited for optimization to avoid restricting the follicle growth (Fig.1b). To mimic the psychological size and shape of the ovary, we produced a positive photosensitive resin mold where the PDMS was poured and dried. Then, the PDMS mold was dissociated and filled with gelatin microspheres to cast GelMA. After crosslinking of GelMA, the hydrogel with gelatin microspheres was dissociated and incubated at 37℃ to dissolve the gelatin microspheres. The micro-cavity ovary was accomplished, followed by implanting immature follicles. Under appropriate culture conditions, the micro-cavity ovary would recapitulate the *in vivo* ovary development from 3 weeks to puberty (Fig.1c). Multiple biological evaluations at organ-cellular levels (Fig.1d) and single-cell levels (Fig.1e) were employed to prove that the micro-cavity ovary enabled follicles to mature, ovulate, and fertilize.

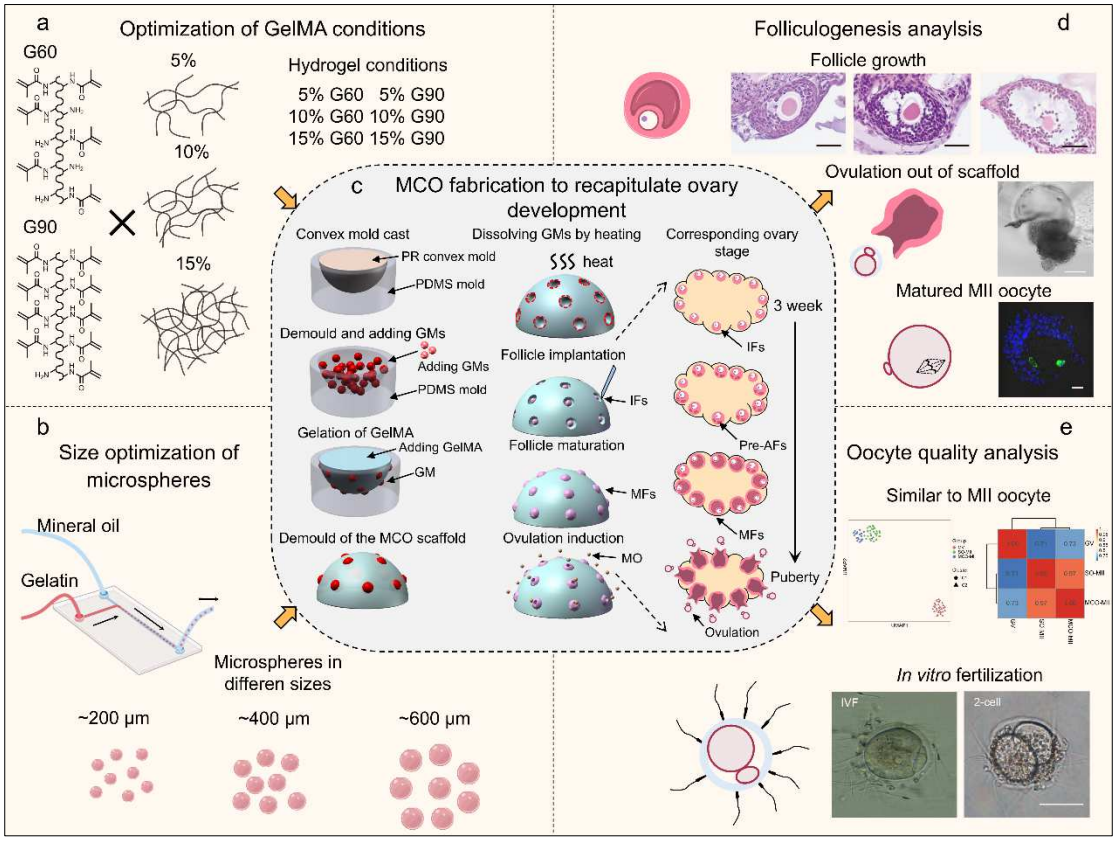

Figure 1. The strategy of the micro-cavity ovary fabrication and function analysis. **a**. Optimization of GelMA concentrations and substitution of degrees of methacryloyl for the micro-cavity ovary, G60 and G90: GelMA 60 and GelMA 90. **b**. Optimization of the size of gelatin microspheres for the micro-cavity ovary. **c**. The fabrication scheme of the micro-cavity ovary and the corresponding *in vivo* ovary stages. MCO: micro-cavity ovary; PR: photosensitive resin; GM: gelatin microsphere; IF: immature follicle; Pre-AF: pre-antral follicle; MF: matured follicle; MO: MII oocyte. **d**. The characterization of follicle maturation. The scale bar was 20 μm. **e**. The characterization of the quality of ovulated oocytes. The scale bar was 50 μm.

Optimization of GelMA concentrations and substitution of degrees of methacryloyl

Ovaries consist of lots of round-shape follicles aligned in an organized manner near the surface, and each follicle grows independently in the ovary. These follicles were supported by a complex extracellular matrix (ECM) which maintained a constant mechanical strength; thus, the mechanical property of GelMA should be optimized to be suitable for follicles. The concentration and degree of substitution of methacryloyl of GelMA will dramatically affect its mechanical strength, thus, it should be optimized. For evaluating GelMA conditions, we employed microfluidic technology to produce gelatin spheres with the size of 600 μm, which was larger than antral follicles, to create the culturing cavity for individual follicles in a 12-plate (Fig. 2a). Before culturing follicles in microcavities, we compared the stiffness of mouse ovary to GelMA for pre-optimization. The elastic modulus of the ovary was obtained by atomic force microscope (AFM) indentation (the indentation points > 80). We used it as a reference

to optimize the GelMA concentration and substitution of the degree of methacryloyl (the indentation points > 100). We divided the GelMA samples into six groups: the concentration was 5%, 10%, and 15% associated with the substitution of the degree of 60% methacryloyl (GelMA 60, G60) and 90% methacryloyl (GelMA 90, G90). By fitting the curve to the distribution of indented elastic modulus, the result revealed the elastic modulus peak of the ovary located between 10% - G60 and 15% - G60 in Figure 2b, or between 10% - G90 and 15% - G90 in Figure 2c. The individual fitting curve is represented in Figure S1. Meanwhile, the average modulus of ovary was 1.511 ± 0.357 kPa which also located between 10% - G60 (0.253 ± 0.128 kPa) and 15% - G60 (2.62 ± 0.766 kPa), or between 10% - G90 (0.904 ± 0.155 kPa) and 15% - G90 (1.91 ± 0.041 kPa) (Fig. S2). The result indicated that 10% or 15% of GelMA might be suitable for follicle culture. To confirm this finding, we created a cavity for culturing follicles by using microspheres with the six different conditions of GelMA. Follicles obviously increased their sizes in 10% - G60, 15% - G60, 10% - G90, and 15% - G90 conditions (Fig. 2d and 2e). The statistical analysis of follicle sizes and live/death ratio showed that follicles cultured in either 5% - G60 or 5% - G90 conditions had smaller sizes and a higher death rate than those cultured in 10% or 15% conditions (Fig. 2f and 2g). Although there was no significant difference in follicle sizes among 10% - G60, 10% - G90, 15% - G60, and 15% - G90 (Fig. 2f), the 10% - G90 condition was better than others since the percentage of large follicles (> 300 μm diameters) was mildly higher while the death rate was slightly lower than other conditions after ten days culture (Fig. 2g). According to our data, 10% - G90 was screened out for further fabrication of the micro-cavity ovary to retain the ovulation ability.

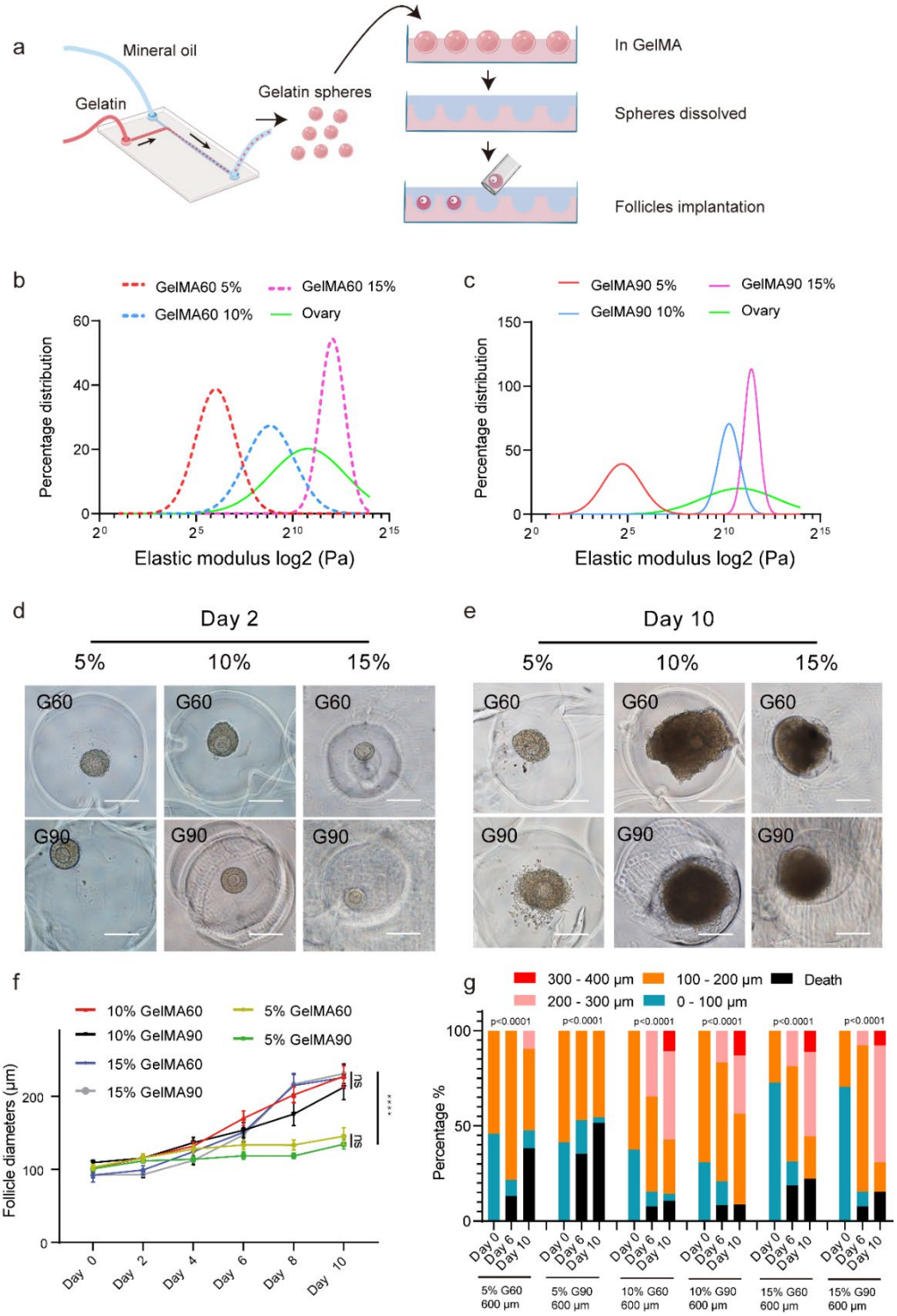

Figure 2. Optimization of different GelMA conditions for the fabrication of micro-cavity ovary. **a**. The strategy for optimizing GelMA conditions in a 12-well plate. **b**. The fitting curve of elastic modulus distribution of mouse ovary and GelMA 60. **c**. The fitting curve of elastic modulus distribution of mouse ovary and GelMA 90. **d**. The follicle was cultured in different GelMA conditions on day 2. The scale bar was 200 μm. **e**. The follicle was cultured in different GelMA conditions on day 10. The scale bar was 200 μm. **f**. The follicle diameter in 10% and 15% GelMA conditions was larger than that in 5% GelMA, $n > 11$, the error bar stands for standard error of mean, the p-value passed two-way ANOVA test, ns: $p > 0.05$; ****: $p < 0.0001$. **g**. The follicle size distribution in different GelMA conditions, the p-value passed Chi-square test, ****: $p < 0.0001$.

The culture cavity created by large gelatin microspheres supported follicle growth and ovulation

The mouse ovarian follicle size ranged from ~100 μm (secondary follicles) to 400 – 500 μm (antral follicles)[31,32] after puberty. The antral cavity occurs when the size is larger than 200 μm, and it is essential for the maturation of oocytes. Therefore, the culture cavity size should be optimized to support the occurrence of the antral cavity. Herein, we used a T-shape microfluidic chip (Fig. S3) to produce gelatin microspheres with diameters of 200 μm, 400 μm, and 600 μm, standing for a small, middle, and large culturing cavity. The same culturing method in Figure 2a was reused to compare their differences. A non-cavity condition was included to evaluate the indispensability of culturing follicles in cavities. Surprisingly, follicles did not attach to the surface of GelMA at the beginning. Even more, granulosa cells dissociated from the follicles after several days of culture (Fig. S4). It might be owing to the horizontal surface of GelMA did not supply ideal physical struts to support follicle attachment. The result of follicle growth in cavities revealed that the average size of follicles cultured in 400 μm and 600 μm cavities were larger than those in 200 μm cavities after ten days of culture. Most importantly, the oocyte was only ovulated in 600 μm cavities after the ovulation induction (Fig. 3a). Although all cavity sizes supported follicle growth, the average size of follicles in 600 μm cavities was larger than other sizes (Fig. 3b). In addition, we found the distribution of sizes was different. All follicles were less than 200 μm when cultured in 200 μm cavities, and the death rate in 200 μm cavities was higher than in others. Large follicles (> 300 μm) were only observed in 600 μm cavities (Fig. 3c). These results implied that the growth and ovulation of follicles required a 600 μm culturing cavity that might be owing to less restriction to granulosa cells expansion.

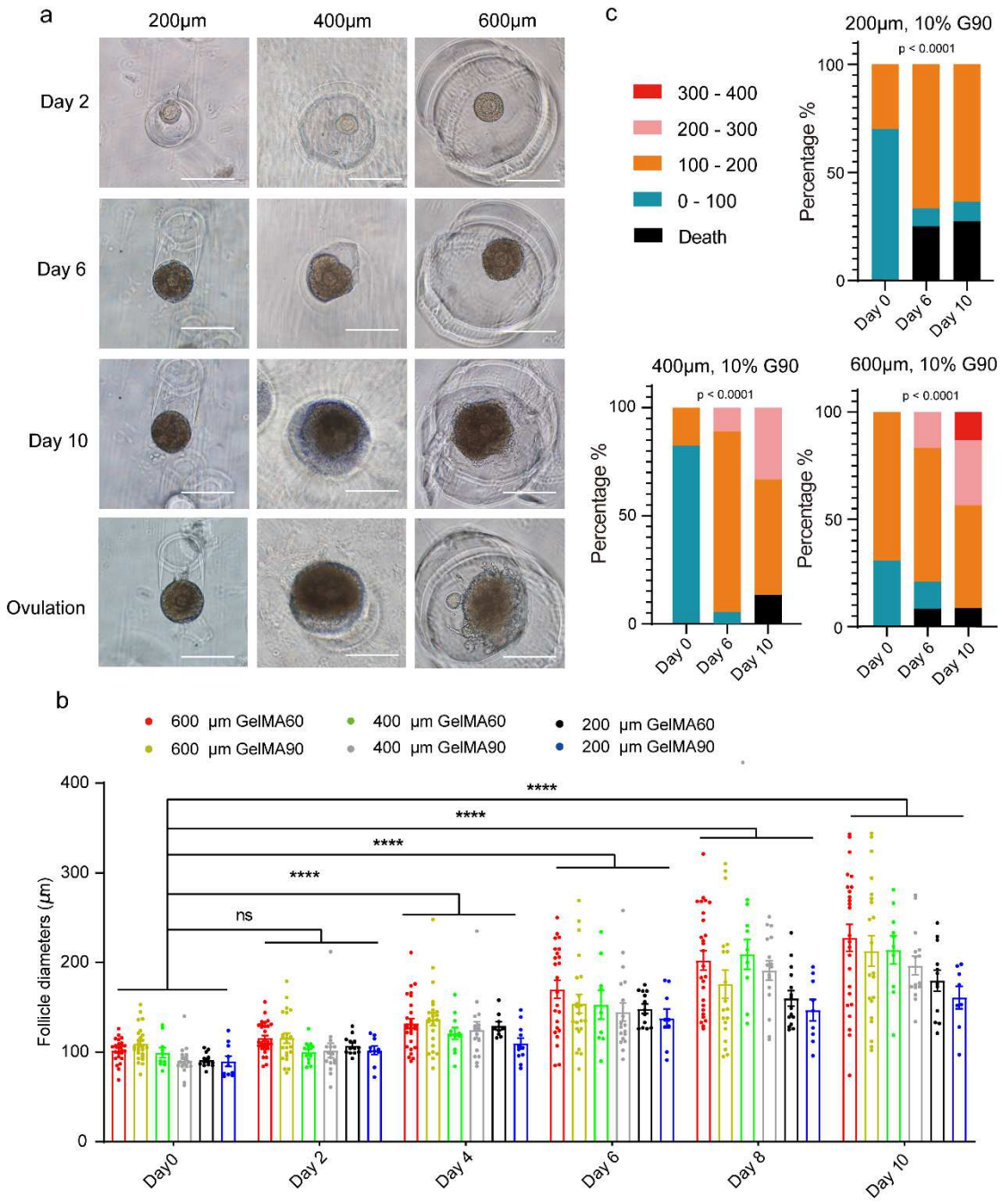

Figure 3. Optimization of the size of gelatin microspheres for the micro-cavity ovary fabrication. **a**. Follicle maturation and ovulation in different sizes of cavities created by gelatin microspheres, the bar was 200 μm. **b**. The statistical summary of the follicle size cultured in different sizes of cavities, n > 8, the error bar stands for standard error of mean, the p-value passed two-way ANOVA test, ns: $p > 0.05$; ****: $p < 0.0001$. **c**. The follicle size distribution cultured in different sizes of cavities, the p-value passed the Chi-square test, ****: $p < 0.0001$.

Fabrication of the micro-cavity ovary scaffold by 10% - G90 and 600 μm microspheres

To mimic the physiological morphology of the ovary for fabrication, the location of follicles was labeled by the Anti-müllerian hormone (Amh) antibody. The staining

result revealed that the follicle grew near the surface in a spotty manner (Fig. 4a, movie S1). To recapitulate the psychological structure, and since the parameter of GelMA and the size of the sphere were determined, mold technology was employed to mimic the morphology of the ovary (Fig. 4B). The gelatin microsphere was labeled by red fluorescence and aligned into the PDMS mold. Then the GelMA was conjugated with green fluorescence and poured into the PDMS mold to cover the microsphere. After gelation, the major volume of the sphere was buried into the GelMA (Fig. 4c). A GelMA structure with microcavities was fabricated by dissolving the microsphere (Fig. 4d). To further identify the growing location of follicles, an intact adult mouse ovary was scanned by scanning electron microscope (SEM) (Fig. S5a). By tearing off a small piece of the surface epithelium of the ovary, the inside cavity was exposed and visualized by SEM, which also indicated that mouse follicles grew under the surface epithelium of the ovary (Fig. 4e, Fig. S5b, and S5c). As for the micro-cavity ovary scaffold, the cavity created by the gelatin microsphere would serve as a nest to support follicle growth and maturation. Besides, an ovulatory opening was left for rupture of the oocyte once the follicle matured (Fig. 4f). All these data confirmed that the gelatin microsphere created a porous surface that would be used to support follicle growth in further study.

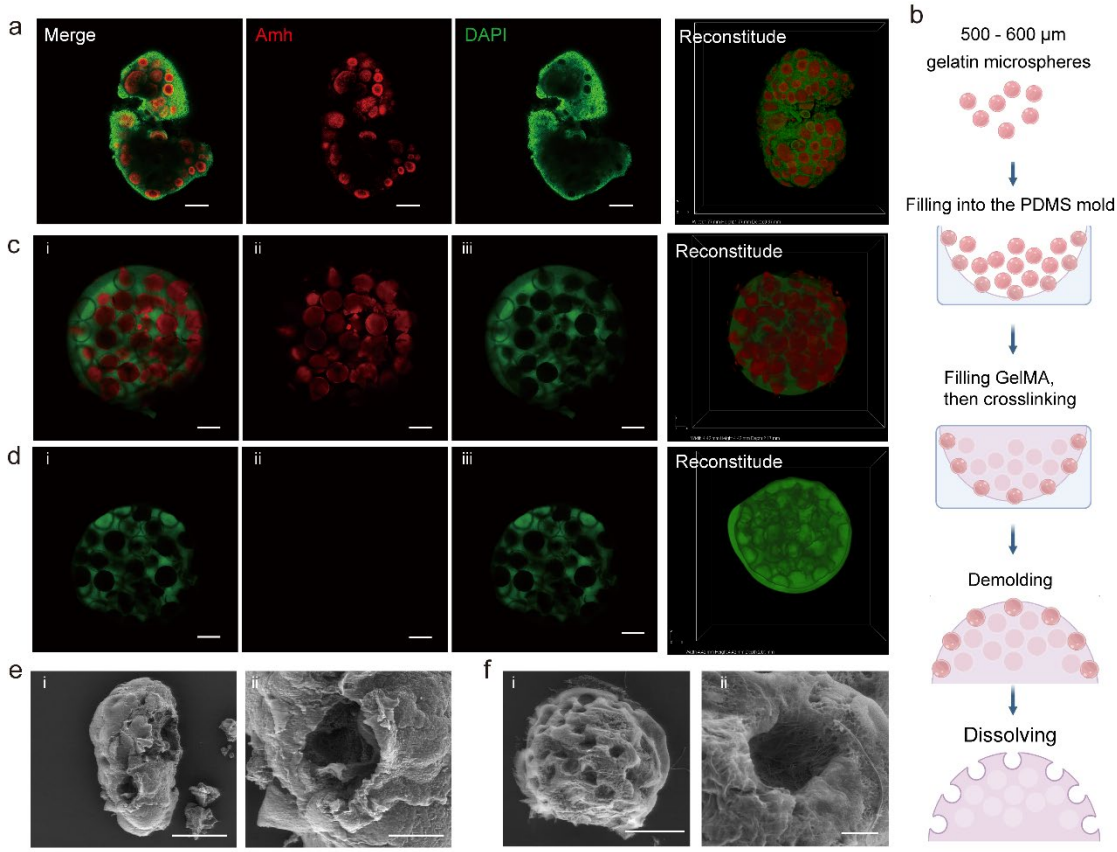

Figure 4. Fabrication of the micro-cavity ovary scaffold. **a**. Amh antibodies identified the physiological structure of mouse ovary follicles. The scale bar was 200 μm. **b**. The strategy of fabricating the micro-cavity ovary scaffold. **c**. The structure of the micro-cavity ovary scaffold with gelatin microspheres, the scale bar was 500 μm. **d**. The structure of the micro-cavity ovary scaffold after the dissolution of gelatin microspheres, the bar was 500 μm. **e**. The SEM image of mouse ovary by tearing off a piece of the surface epithelium, the scale bar was 500 μm (left panel) and 100 μm (right panel). **f**. The SEM image of the micro-cavity ovary scaffold after the dissolution of gelatin microspheres, the scale bar was 1mm (left panel) and 100 μm (right panel).

Folliculogenesis within the micro-cavity ovary

Granulosa cell proliferation within the folliculogenesis will expand the follicle size and develop an antrum filled with follicle fluid. We seeded immature follicles into the micro-cavity ovary (Fig. 5a). The SEM was used to scan the cavity with follicles to prove the follicle adhering and sprouting inside the cavity rather than in other places (Fig. 5b). Then, the increased size and a clear antrum cavity were identified after seven days of culture (Fig. 5c). The histology results represented a complete stage of folliculogenesis from secondary follicles to antral follicles (Fig. 5d). Next, we questioned whether the marker of granulosa cells and oocytes was normally expressed. Amh and deleted in azoospermia like (Dazl) were stained for they are only expressed in granulosa cells and oocytes, respectively[33,34]. Our staining result showed that Amh and Dazl were expressed separately in granulosa cells and oocytes (Fig. 5e). As observed above, an antrum cavity was visualized by the 3D reconstitution through a confocal microscope scanning (Fig. 5f, movie S2). Several female hormones were

analyzed to verify the micro-cavity ovary's hormone secretion ability. Estradiol was undetectable at onset, then increased to 36.3 ± 17.0 ng/ml on day 10 (Fig. 5g). Similarly, Amh was undetectable on day 1, then increased to 0.878 ± 0.418 ng/ml after ten days of culture (Fig. 5h). Other hormones, Inhibin-A, and Inhibin-B, which participated in the hypothalamic-pituitary-ovary (HPO) axis, also increased from an undetectable level to 1.745 ± 0.259 ng/ml (Fig. 5i) and 0.392 ± 0.103 ng/ml (Fig. 5j), respectively. According to our results, the data confirmed that follicle growth and hormone secretion occurred within the micro-cavity ovary.

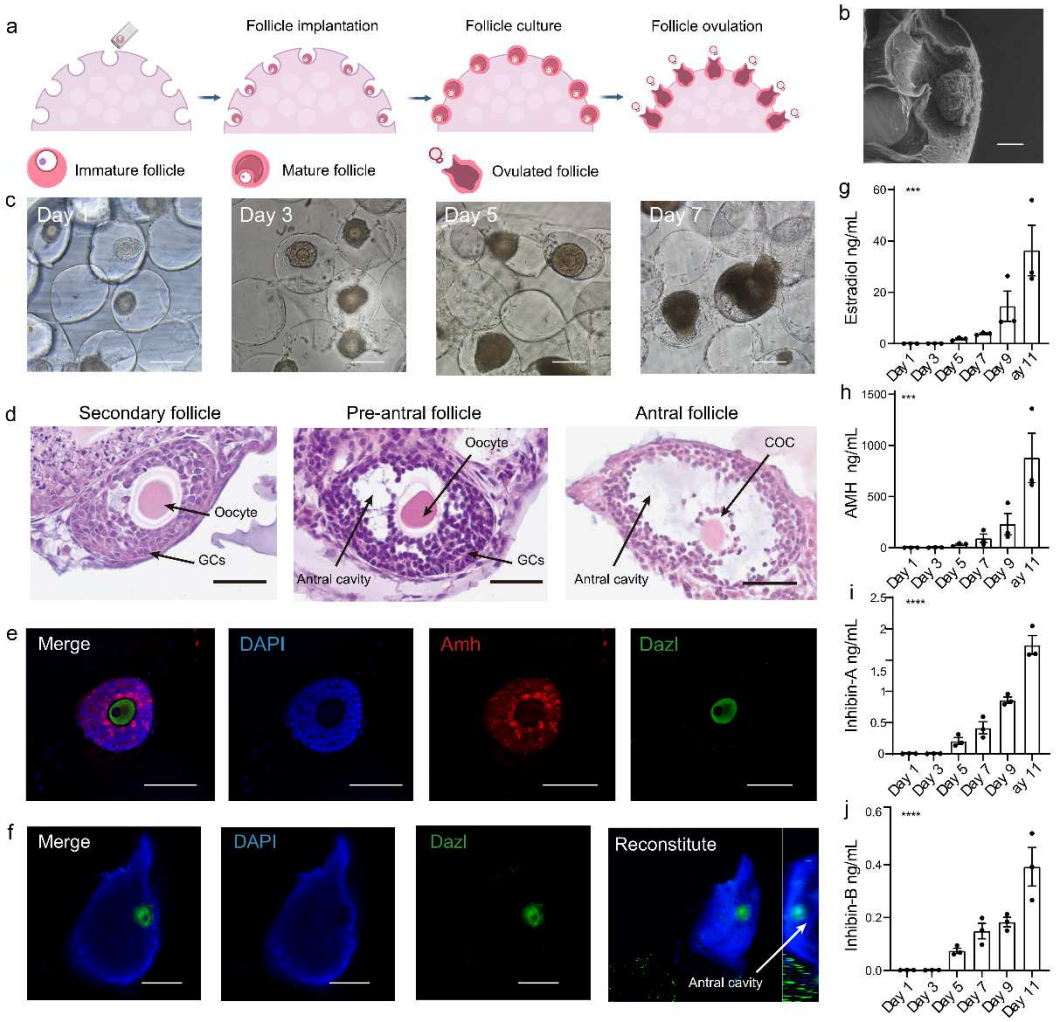

Figure 5. Characterization of folliculogenesis within the micro-cavity ovary. **a**. The scheme for culturing follicles within the micro-cavity ovary. **b**. SEM visualized the follicle to confirm its growing location within the cavities. The scale bar was 50 μm. **c**. The follicle increased their sizes within the micro-cavity ovary from day 1 to day 7. The scale bar was 200 μm. **d**. The H&E histological analysis of folliculogenesis from the secondary follicle to the antral follicle. GCs: granulosa cells; COC: cumulus-oocyte complex, the scale bar was 50 μm. **e**. Amh and Dazl were expressed by granulosa cells and the oocyte, respectively. The scale bar was 100 μm. **f**. The antral follicle was reconstituted by confocal images. **g – j**. Female hormones: mouse estradiol, mouse AMH, mouse Inhibin-A, and mouse Inhibitin-B were expressed within the micro-cavity ovary, n = 3, the error bar stands for standard error of mean, and the p-value passed the one-way ANOVA test, ***: $p < 0.001$; ****: $p < 0.0001$.

Ovulation within the micro-cavity ovary

Ovulation is a dynamic tissue remodeling process that involves degradation of extracellular matrix (ECM), rupture of follicular layers, and release of mature oocytes, therefore, serving as a huge challenge for ovary fabrication. Distinguishing from the conventional scaffold, the micro-cavity ovary supported the rupture of matured MII oocytes *in vitro*. To verify the micro-cavity ovary restoring the ovulation ability, follicles were seeded in the ovary and cultured in a living cells workstation. After triggering the ovulation, the dynamic morphology of follicles was recorded per 25 min to monitor the ovulation process. Follicles did not change during the first 7 hours of cytokines' treatment. It was clearly observed that the cumulus-oocyte complex (COC) was extruded out of the micro-cavity ovary within the next 6 hours (Fig. 6a). The released COC floated in the medium rather than encapsulated by the hydrogel (Fig. S6). These data indicated the ovulation function of the biomimetic ovary was recovered. Additionally, the extruded oocyte was collected to examine the competence of meiosis. The polar body and the spindle structure were identified, indicating the fully matured MII oocyte has been ovulated (Fig. 6b). To expand the potential application of the micro-cavity ovary, we questioned whether the ovulated oocyte was fertile. Spontaneous parthenogenesis occurred in a prolonged culture with the presence of hCG and mEGF (Fig. 6c). More directly, the IVF was performed. The result revealed that the ovulated oocyte started to cleave into a 2-cell stage around 12h after the end of IVF (Fig. 6d).

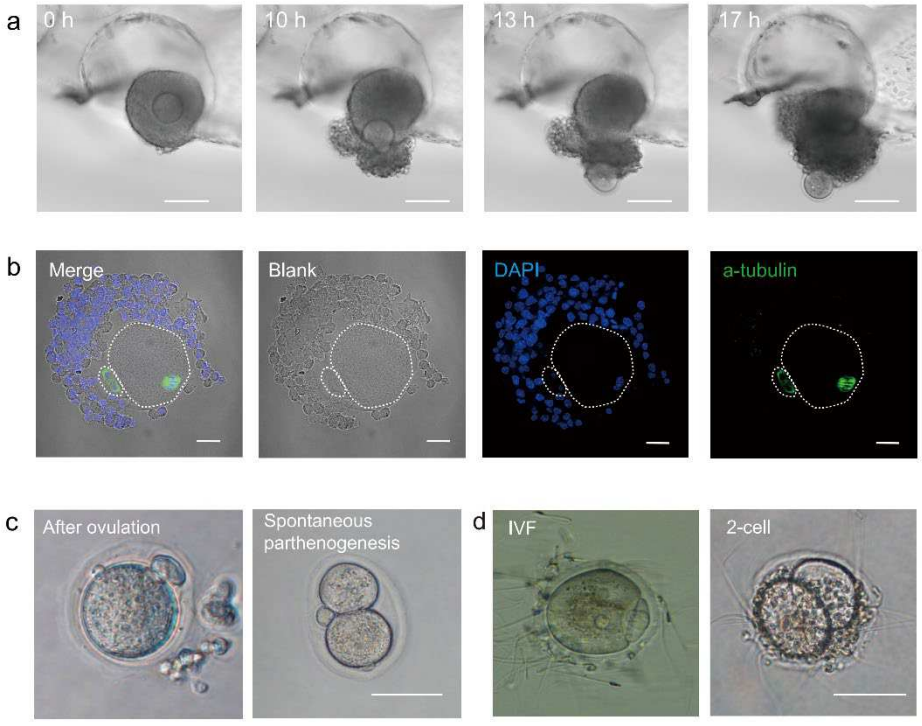

Figure 6. Characterization of the ovulation process within the micro-cavity ovary. **a**. The time-lapse record of the entire ovulation process, the bar was 100 μm. **b**. The ovulated oocyte was in the meiosis matured stage. The scale bar was 20 μm. **c**. The spontaneous parthenogenesis of the ovulated oocyte. The scale bar was 50 μm. **d**. The ovulated oocyte developed to the 2-cell stage after IVF. The scale bar was 50 μm.

The single-cell RNA-seq revealed the transcriptome of the MCO-MII oocyte was similar to the corresponding stage of *in vivo* oocytes

To characterize the ovulated oocytes from the micro-cavity ovary, we sequenced 22 single MII oocytes from the micro-cavity ovary, 30 single MII oocytes from the super-ovulated mouse, and 30 germinal vesicle (GV) oocytes from P16 mouse before transplantation to the biomimetic ovary. After stringent filtering, 21 micro-cavity ovary MII (MCO-MII) oocytes, 30 super-ovulated MII (SO-MII) oocytes and 30 GV oocytes were retained for further analysis. On average, 8812 genes, 8516 genes, and 12370 genes were identified from MCO-MII, SO-MII, and GV oocytes as shown in Figure S7a. Oocytes samples obtained from different mice were mixed well and showed no batch effect in the uniform manifold approximation and projection (UMAP) plot (Fig. S7b). Unique molecular identifier (UMI) transcripts were examined in each sample, showing no obvious differences among the same group (Fig. S7c). We also examined the expression of mitochondrion genes to exclude the contamination (Fig. S7d). These data suggested the sequencing result was of great quality for further analysis. 2 clusters were identified in the UMAP plot. In this plot, MCO-MII oocytes and SO-MII oocytes were divided as cluster 1, while GV oocyte was divided as cluster 2 (Fig. 7a). Markers of ectoderm, mesoderm, endoderm and germ cells were examined to confirm the samples expressing oocyte markers as shown in feature plot (Fig. S7e). Early folliculogenesis genes, such as *Nobox* and *Tnni3*, were maintained at a higher level in GV oocytes (Fig. S7f) whereas early embryo development-related genes were higher in MCO-MII and SO-MII oocytes (Fig. S7g).

Next, the Pearson correlation was performed to evaluate the similarity among GV, SO-MII, and MCO-MII oocytes (Fig. 7b). The result revealed that the correlation between SO-MII and MCO-MII oocytes was 0.97, higher than that of SO-MII versus GV (correlation was 0.72) and MCO-MII versus GV (correlation was 0.74). This result indicated a high similarity between SO-MII and MCO-MII oocytes. Furthermore, the putative chromosome ploidy (PCP) value was evaluated. Compared to the SO-MII oocyte, the MCO-MII oocytes showed the same chromosome ploidy, while the GV oocyte showed the ploidy was double (Fig. 7c), supporting MCO-MII oocytes finishing the first cleavage of meiosis as shown in Figure 6b. Moreover, for a particular oocyte stage, if some of the MCO-MII oocyte's differential expressed genes (DEGs) and SO-MII oocyte's DEGs participated in the same biological process, these shared genes and biological processes would provide valuable information to evaluate the similarity between them. Therefore, we performed a scatter plot to show that the DEGs of SO-MII versus MCO-MII oocytes (Fig. 7d) was less than that of DEGs obtained from SO-MII versus GV oocytes (Fig. 7e) or MCO-MII versus GV oocytes (Fig. 7f). Furthermore, Heatmap based on DEGs of SO-MII versus GV (Fig. 7g, Table S1) or MCO-MII versus GV (Fig. 7h, Table S2) presented distinct cell types and indicated MCO-MII oocytes and SO-MII oocytes shared the major DEGs. In total, 1347 shared DEGs were identified between SO-MII and MCO-MII oocytes (Fig. 7i). To evaluate their similarities, we divided SO-MII or MCO-MII oocytes into 2 groups (10 oocytes each) and obtained the share DEGs between groups by separately comparing them to GV

oocytes. Hundreds of DEGs were varied even in the same MII oocyte sample (Fig. S8a and S7b), supporting that 1347 shared DEGs reflecting a strong similarity between SO-MII oocytes and MCO-MII oocytes. Then, we performed gene ontology (GO) and found that over half of GO terms were shared by MCO-MII and SO-MII oocytes (Fig. 7j, Fig. S8c – S8f, Table S3 – S6). The shared DEGs between MCO-MII and SO-MII oocytes provided clear clues regarding whether they were in the same developmental stage. We found genes related to metabolic biological processes were degraded in MCO-MII and SO-MII oocytes (Fig. 7k). On the other hand, genes related to cell cycle and histone modification, etc., were accumulated in SO-MII and MCO-MII oocytes (Fig. 7l). These results indicated that MCO-MII oocytes were quite similar to SO-MII oocytes.

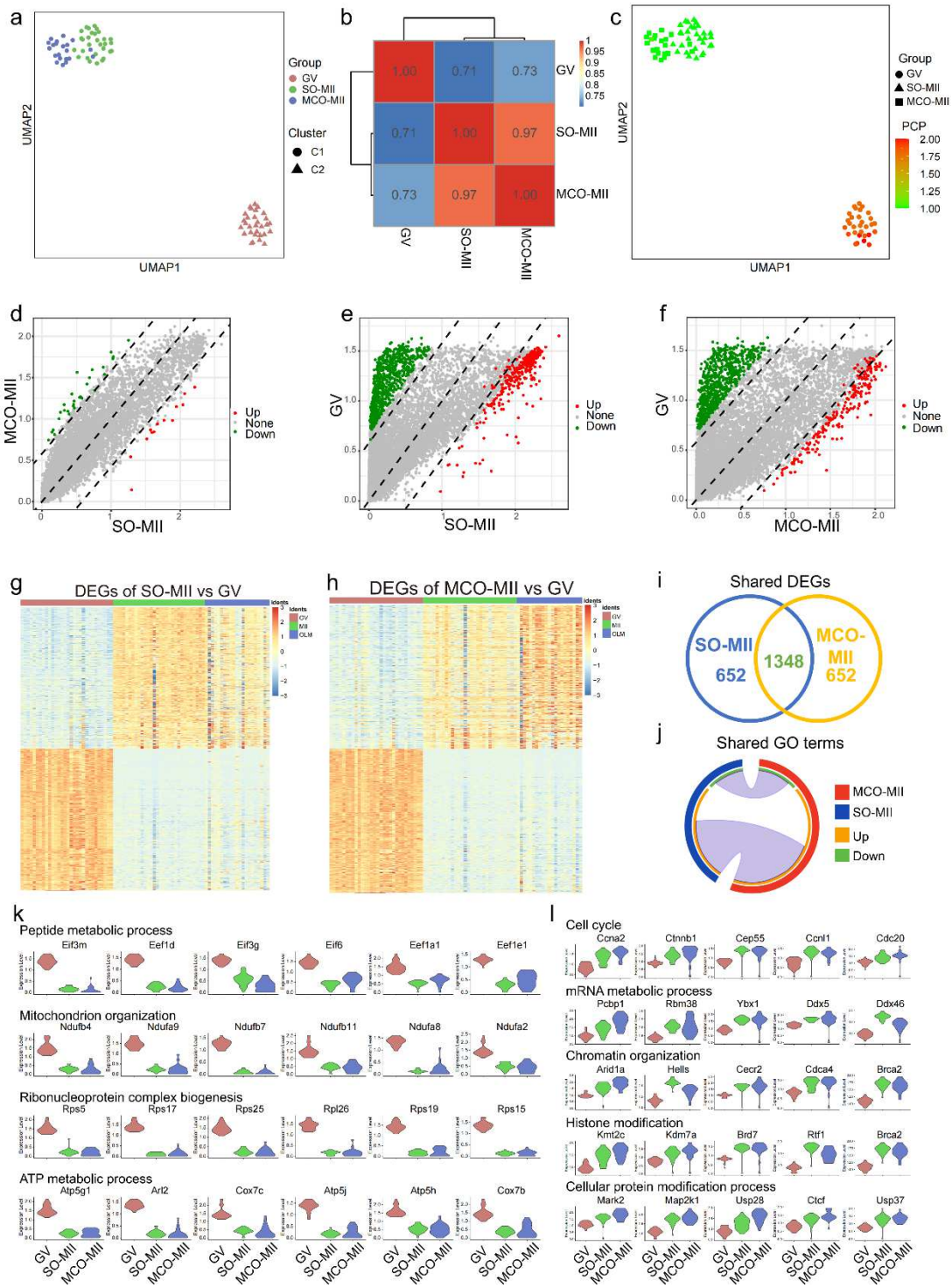

Figure 7. Single-cell RNA-sequencing of GV, SO-MII, and MCO-MII oocytes. **a**. Cell cluster analysis by UMAP plot. **b**. Pearson correlation analysis of GV, SO-MII, and MCO-MII oocytes. **c**. The putative chromosome ploidy value of GV, SO-MII, and MCO-MII oocytes. **d**. Scatter plot between SO-MII and MCO-MII oocytes. **e**. Scatter plot between GV and SO-MII oocytes. **f**. Scatter plot between GV and MCO-MII oocytes. **g**. Heatmap of DEGs obtained from SO-MII versus GV oocytes. h. Heatmap of DEGs obtained from MCO-MII versus GV oocytes. **i**. VENN map of shared DEGs between SO-MII and MCO-MII oocytes. **j**. Circos plot of shared GO terms between SO-MII and MCO-MII oocytes. **k**. Down-regulated genes in SO-MII and MCO-MII oocytes. **l**. Up-regulated genes in SO-MII and MCO-MII oocytes.

Genes that differently expressed in SO-MII and MCO-MII oocytes indicated the clues for further optimization

Although the germ cell-related genes' expression was similar, we also identified some variable-expressed genes between MCO-MII and SO-MII oocytes that might be caused by the difference between *in vivo* ovary environment and the micro-cavity scaffold niche (Fig. 8a). The GO analysis was also performed to present their differences (Fig. S9). In these genes, apoptosis inhibition marker *Xaf1* was at a high level (1.5-fold) in SO-MII oocytes, implying natural ovulated MII oocytes might be more resistant to apoptosis. On the contrary, *Yap1* was 1.2-fold higher in MCO-MII oocytes. Probably because of the expression of *Yap1*, stem cell maintenance genes were ectopic activated, such as *Nfya* and *Lin28a*. A protein relation network analysis was performed among the top 10 DEGs. The result indicated that *Xaf1* in SO-MII oocytes (Fig. 8c) whereas *Yap1* in MCO-MII oocytes (Fig. 8d) might serve as the center factors causing the difference. As a control, the top 10 DEGs of GV oocytes were also analyzed that these genes involved in ribosome biogenesis (Fig. 8b). Since *Yap1* is involved in the Hippo pathway that regulates the cell elasticity in response to the mechanics of extracellular matrix (ECM)[35]. These findings suggested that, although the modulus of the micro-cavity has been optimized, other properties should be further optimized to reduce the ectopic genes such as *Yap1*.

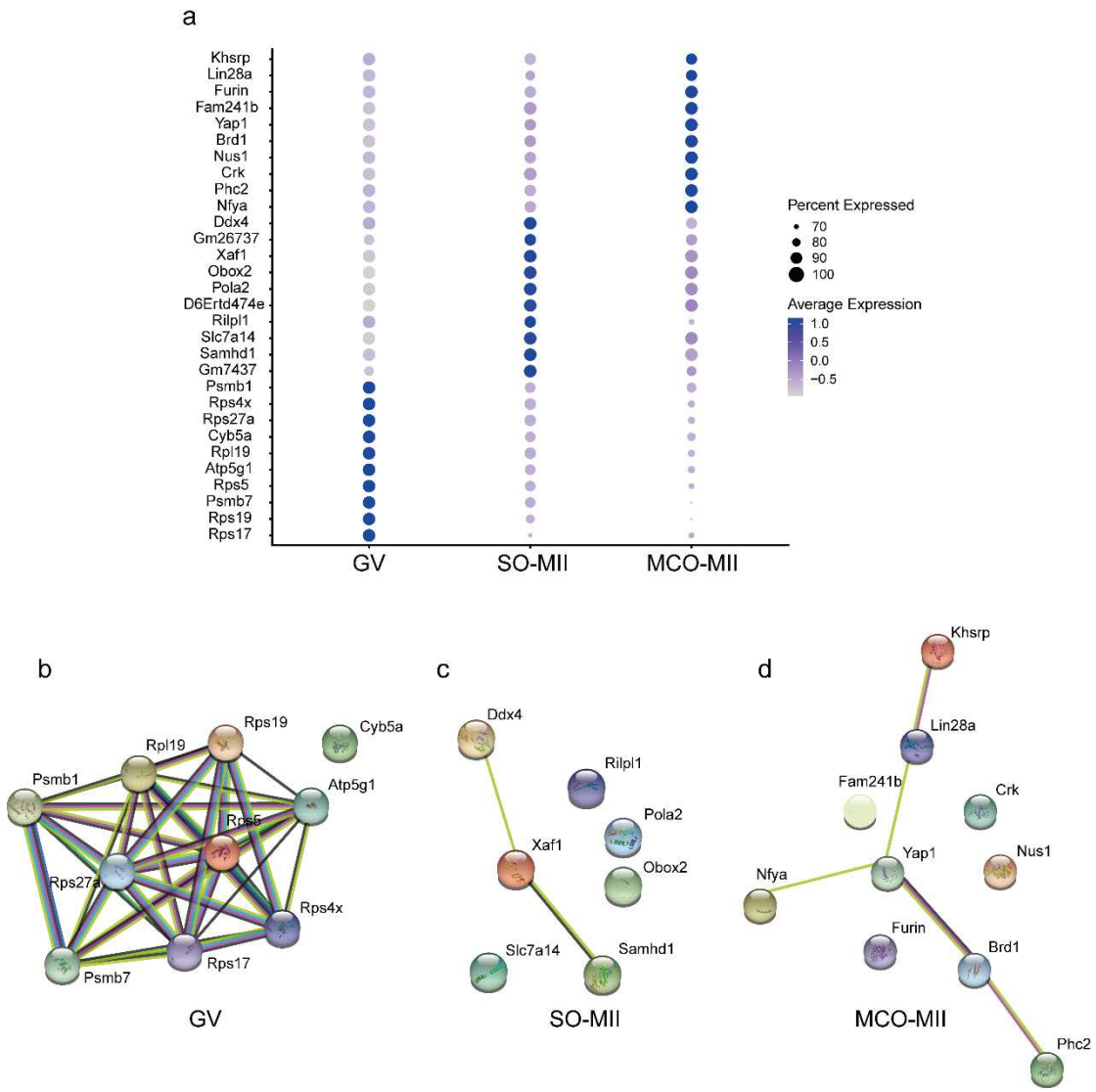

Figure 8. DEGs might affect the oocyte status. **a**. Top 10 DEGs of GV, SO-MII, and MCO-MII oocytes. **b**. Protein network analysis of top 10 DEGs in GV oocytes. **c**. Protein network analysis of top 10 DEGs in SO-MII oocytes. **d**. Protein network analysis of top 10 DEGs in MCO-MII oocytes.

Discussion

A basic understanding of organogenesis was that the organ's structure was mutually adapted to its function. Since the matured follicle is always located around the ovary's surface, we followed this rule, fabricated the micro-cavity ovary, and demonstrated that by mimicking the phenomenon of follicles growing around the surface, it could facilitate the biomimetic ovary to retain its ovulation ability. Although some organ-like tissues were developed by organoids differentiation or bioengineering technologies, such as kidney tissues[36,37], heart tissues[38-46], and gut tissues[47,48], many of them did not involve in complex organ processes or recapitulating the elegant structure of the organ. Our study gave a highly controllable and easy-to-fabricate approach to build a physiological-like ovarian model that is therefore promising for developing therapeutic transplantation strategies.

Although the micro-cavity ovary left openings for the release of the oocyte, we surprisingly found that the ovulation ability was highly related to the microcavity size. We observed the ovulated oocytes only if the microcavity size was larger than the growing follicle. Otherwise, the small size of the microcavity wrapped the follicle and disturbed its maturation. When the cavity size was set as 400 μm, the follicle also seemed to be non-responsive to the stimulus of chorionic gonadotropin, although the reason remained unknown. Moreover, we also reported that the stiffness of the hydrogel was significant in supporting follicle maturation. As the stiffness and the microcavity size belong to the mechanical property of hydrogels, our biomimetic ovary had the potential to be fabricated to improve its biocompatibility by varied bio-materials with or without ovarian somatic cells instead of the GelMA we used.

Since the microfluidic was able to produce anisotropic microparticles[49], the application potential of the micro-cavity ovary could be further enhanced. However, when comparing our results to those of follicles under physiological conditions, the shape of the follicle that grew in the micro-cavity ovary seemed to be asymmetric and irregular. The reason might be that the contact surface between follicles and the micro-cavity ovary was asymmetric, resulting in uneven support to the granulosa cell expansion. Thus, one promising solution was designing and producing anisotropic microparticles to modify the growing cavity, making it more suitable for follicle growth.

One of the critical aspects of this study was that we recorded and proved the biomimetic ovary recovered the ovulation ability. Our data gave shreds of evidences to support the possibility of rebuilding the functional organ through the engineering design. The *in vivo* ovulation process determined the mature oocyte's release, then finally affected the success of the fertilization. In conventional 3D culture methods, ovarian follicles were encapsulated in hydrogels. The hydrogel completely restricted the ovulation path; therefore, the oocyte was usually isolated by mechanical dissociation or enzymic digestion. In contrast to the previous 3D printed ovarian scaffold[50,51], our micro-cavity ovary directly proved to restore the ovulation ability and supported the maturation of the individual follicle instead of a cluster of multiple follicles. The whole ovulation process could be entirely monitored under a microscope which may assist in investigating the unknown mechanism of reproductive diseases, such as the appearance of atretic follicles. Moreover, the micro-cavity ovary was easy and rapid to be fabricated independently of an expansive, precision 3D printing machine to save the cost.

In pioneering studies, multiple bio-fabricated reproductive organs were summarized[52], including the fallopian tube, uterus, and ovary. However, many unsolved questions remained from ovulation to blastocyst implantation, for these processes happened *in vivo* as a black box. None of the dynamic models that integrated multi-reproductive organs was fabricated to repeat these *in vivo* processes for study. In our results, the micro-cavity ovary overcame the barrier of difficulty in observing, allowing the rupture of matured MII oocytes. Moreover, the ovulated oocyte was meiosis maturated and fertilized. In addition, the micro-cavity ovary secreted multiple hormones, including

Amh, Inhibition-A/B, and estradiol. These increased hormones indicated that the micro-cavity ovary might have the potential to balance the hormonal feedback loop of the hypothalamic-pituitary-ovary (HPO) axis in an *in vitro* system. According to our results, the data suggested a vast advantage of the micro-cavity ovary in fabricating *in vitro* models. Combined with artificial organs such as fallen tubes, it has the potential to recapitulate the whole reproductive process in a chip, therefore, becoming an important tool in drug discovery, mechanism study, and ovary substitute for transplantation.

To qualify the ovulated oocyte, we used single-cell RNA-seq analysis to characterize its quality. At the molecular level, the ovulated oocyte was more similar to the *in vivo* MII oocyte. The Pearson clustering, UMAP plot, and heatmap of DEGs revealed the ovulated oocytes from micro-cavity ovary were close to the *in vivo* SO-MII oocytes. The PCP value also supported MCO-MII oocytes were meiosis matured. We pointed out multiple important genes, involving in regulating the oocyte maturation, were differently expressed in MCO-MII oocytes and GV oocytes. To our knowledge, oocytes started the meiosis and finished the duplicate of DNA at the onset of folliculogenesis[53]. Then the oocyte arrests the meiosis and starts to accumulate mRNA for maturation. Thus, compared to the SO-MII oocyte, GV oocytes preferred to express metabolic-related genes. In our studies, we identified multiple NADH-ubiquinone oxidoreductase and ATP synthase family genes were higher in GV oocytes, indicating a high energy consumption within GV oocytes. Moreover, eukaryotic translation initiation and elongation factors were identified with high expression in GV oocytes giving a strong hint that the protein synthesis was activated[54,55]. In response to this, ribosomal proteins were also highly expressed to participate the protein synthesis. These data suggest that GV oocytes might initiate specific proteins synthesis needed for maintaining the growing state or for preparing for the resumption of meiosis. As the oocyte matured, the maturation promoting factor (MPF) was activated by LH surge, inducing chromosome segregation and extrusion of the first polar body[56]. As the effect of meiosis resumption, the dominated expressed gene shifted from metabolic genes to meiosis-related genes, for example, *Ccna2* and *Cep55* were highly expressed in MII oocytes in our study.

When compared the MCO-MII oocytes to the SO-MII oocytes, major germ cell-related pathways and markers showed few differences, however, we also identified several DEGs that might indicate the micro-cavity scaffold should be further optimized. *Xaf1* was identified as a strong tumor suppressor[57,58] which was ubiquitously expressed in normal tissues but not in many cancer cells[59]. Overexpression of *Xaf1* induced ovarian cancer apoptosis[60], but it was unknown about the exact function in oocytes. Our data found the level of *Xaf1* in SO-MII oocytes was higher than that in MCO-MII oocytes, suggesting the SO-MII oocytes might be more resistant to apoptosis than MCO-MII oocytes. In MCO-MII oocytes, *Yap1* was maintained a high level than its in SO-MII oocytes. *Yap1* encodes the yes-associated protein (Yap), participates in Hippo pathway that controlling organ growth, stem cell self-renewal and cell differentiation[61]. Yap is regulated by mechanical cues, i.e. the rigidity, strain, shear stress, or adhesive area of

ECM[35]. Although we optimized the modulus of GelMA before the fabrication, the high level of *Yap1* in MCO-MII oocytes might indicate that multiple mechanical properties not only the modulus of the scaffold should be considered and further optimized to reduce *Yap1* expression. Probably due to the abnormal expression of *Yap1*, several DEGs, such as *Lin28a*, might be affected. In addition, the translocation of Yap1 between cytoplasm and nucleus results in activation of different pathways[62], therefore, the location and expression of Yap1 in MCO-MII oocytes should be further determined.

Taken together of our data, we provided a novel, easy-to-fabricated method to build a biomimetic micro-cavity ovary. Within the micro-cavity ovary, it supported folliculogenesis, steroidogenesis, and oogenesis. Moreover, our data directly confirmed the micro-cavity ovary restored the ovulation ability based on an engineering design, which could be further applied in clinic research.

Methods

Fabrication of the T-shape microfluidic device and microspheres production

SYLGARD 184 silicone rubber kit (DOW) was used to make a T-shape microfluidic chip. The two liquids were mixed in a beaker at a 10:1 ratio and stirred with a glass rod for at least 6 minutes. The mixed liquids were transferred to customized chip molds. Two steel needles were buried into the PDMS to form a T-shape channel. Then, the mixture was cross-linked in a drying oven at 45°C overnight. Then, the cured T-shape microfluidic chip was demolded (length: 25 mm, width: 15 mm, height: 10 mm). The diameter of the T-shape channel was restricted to the diameter of the needle, controlling the diameter of microspheres. Next, 7.5% w/v gelatin (Sigma, V900863) and oil phases (Sigma, M8410) with 2% v/v Span80 were pumped into the chip from the different sides with a velocity ratio of 1:5. The microsphere passed through an ice box to gelatinize the gelatin. Then, microspheres were collected in 15 ml centrifuge tubes and washed five times with pre-cooled PBS to replace the oil.

Synthesis of fluorescent gelatin

Rhodamine-conjugated gelatin can be obtained by reacting NHS-rhodamine (46406 Thermo Scientific) with gelatin. Gelatin was fully dissolved in phosphate buffer solution（PH ≈ 8.1）at 50℃ to prepare 10 wt% solution. After dissolving, NHS-rhodamine was added into gelatin solution (30 mg of NHS-rhodamine for every gram of gelatin) and reacted for 3 hours in dark with stirring and heating (50℃). Then the mixture was transferred to dialysis for 5-7 days with pure water at 40℃, followed by freeze-drying and stored at -20℃.

Fabrication of the micro-cavity ovary

The GelMA was bought from commercial products (EFL, EFL-GM-60, EFL-GM-90). The solution was prepared as 5%, 10%, 15% GelMA60 or GelMA90 with 0.25% LAP. The ovarian-like convex mold was designed by SolidWorks software. The size of the convex mold was 3mm in diameter, ovarian-like shape. Then a concave PDMS mold

was then obtained by peeling it off the convex mold. Next, we poured gelatin microspheres and GelMA into the PDMS mold, then the GelMA was crosslinked at 30 mW/cm^2 for 30s to fabricate the micro-cavity ovary scaffold. After gel demoulding, the micro-cavity ovary scaffold was incubated at 37℃ to dissolve microspheres. Then the culture cavity was exposed and waiting for seeding ovarian follicles.

Collection of P16 mouse follicles and seeding to the scaffold

P16 mouse follicles were collected from CD1 mice based on established protocol[63]. In brief, the P16 CD1 mouse was sacrificed, and the ovary was obtained and transferred to L-15 medium (Sigma, L1518) with 5% FBS. The immature follicle was mechanically dissociated. P16 immature follicles with healthy morphology were collected. Then, the isolated follicles were seeded to the cavity within the micro-cavity ovary by narrow-tipped pipettes.

***In vitro* maturation of P16 mouse follicles**

The culture medium was prepared as the published protocol[64]. In brief, the maturation medium was composed of α-MEM (Gibco, 12571063) supplemented with 5% FBS, 0.1 IU/ml FSH (Sigma, F4021), 5 μg/ml insulin, 5 μg/ml transferrin, 5 ng/ml selenium (Sigma, 11074547001). The follicle was incubated at 37℃, 5% CO_2 in air. Half of the maturation medium was changed every day till the antral cavity was observed.

Ovulation induction and spontaneous parthenogenesis

The ovulation induction medium was composed of the maturation medium with 10 ~ 30 IU/ml chorionic gonadotropin for horses and 10 ng/ml mEGF (Peprotech, 315-09), incubating follicles at 37℃, 5% CO_2 in air for 16h ~ 18h. The oocyte spontaneously divided to a 2-cell stage for a further 24h of culture.

Measurement of the diameter of follicles and the death/live ratio

The distance that divided the follicle into two symmetrical parts was measured. The distance must span the center of the oocyte. The death/live ratio was measured according to the intact morphology of follicles and oocytes.

Oocytes collection

GV oocytes were obtained from P16 CD1 mouse ovary. In brief, the P16 CD1 mouse was sacrificed, and the ovary was removed to L-15 medium (Sigma, L1518) with 5% FBS. The secondary follicle was mechanically dissociated. Then, GV oocytes were released by puncturing the follicles with a 30 G sterile needle under a stereomicroscope. MII oocytes were collected from 4-week CD1 mouse. Mice were injected of 10 IU pregnant mare serum gonadotropin (PMSG). Then, these mice were injected of 10 IU hCG 47h later. After 16h of the injection of hCG, the MII oocyte was collected. MCO oocytes were performed IVM as described in this study, and the matured oocytes with first polar body were collected.

IVF procedure

The 8-week male mouse was sacrificed, and the epididymis was obtained. The epididymis was cut 3 – 4 times and transferred to HTF medium (Sigma, MR-070) to harvest matured sperms. After one hour of sperm capacitation, sperms and oocytes were co-incubated for 4h ~ 6h at 37℃, 5% CO_2 in air. Then sperms were washed, and the fertilized oocyte was transferred to the KOSM medium (Sigma, MR-101-D). The zygote was going to start cleavage within 12h.

Time-lapse record of the ovulation process

Follicles within the micro-cavity ovary were transferred into a 35mm dish. Then, the dish was transferred into a NIKON TI2 live-cell workstation at 37℃, 5% CO_2 in air for 24h. The ovulation process was recorded per 25min to form a time-lapse movie.

The elastic modulus test by AFM indentation

The ovary or GelMA was plated at the center of a 60mm dish and soaked by DPBS (Hyclone, SH30028.01) at room temperature. The AFM used in our experiments is the MFP-3D™ Stand Alone AFM (Asylum Research) to optically align the probe to the samples. The probe we used was qp-SCONT (NanoAndMore) with a normal spring constant of 0.01 N/m. The cantilever applied the force mode with a predefined force of 1.5nN. The cantilever was calibrated on the glass bottom before the measurements to determine the spring constant. At least three random locations in each sample were probed, and 36 points for each location were indented in an area of 20 × 20 μm. The elastic modulus was automatically calculated by ASYLUM RESERACH software (Version 13.04.77) followed by Oliver-Pharr formula.

SEM image of the micro-cavity ovary

We froze the micro-cavity ovary scaffold at -80℃ overnight. Prior to the freeze-drying process, the freeze dryer was pre-cooled. Then scaffolds were transferred to the freeze dryer before their thawing. The freeze-drying process was performed for 48h. The dried scaffold was mounted to carbon tape and coated with Pt with a Sputter Coater Leica EM ACE600. Images were scanned with a Hitachi S-5500 cold field emission scanning electron microscope**.**

SEM image of the ovary and the follicle within the micro-cavity ovary

The cell sample was fixed with 4% PFA (leagene, DF0133) in DPBS for 30 min. Then we prepared a series of ethanol solutions with 10%, 20%, 30%, 40%, 50%, 60%, 70%, 80%, 90%, and 100% concentrations. Then, the fixed cell sample was soaked in the ethanol solution from a low to a high concentration subsequently for 30 min each. Then the cell sample was dried in air overnight. The dried sample was mounted to carbon tape and coated with Pt using a Sputter Coater Leica EM ACE600. Images were scanned with a Hitachi S-5500 cold field emission scanning electron microscope**.**

Immunofluorescence staining of follicles within micro-cavity ovary

Follicles within the micro-cavity ovary were fixed by 4% PFA in DPBS for 30 min. Then the fixed cell was washed by 1 × TBST for 5 min twice. Then the sample was

soaked in blocking buffer composed of 1 × TBST with 10% donkey serum and 0.1% Triton-X for 1h. Preparing anti-Dazl (BIO-RAD, MCA2336) and anti-Amh (Abcam, ab272221) antibodies at 1 : 100 ratio in blocking buffer and incubating the cell sample at 4℃ overnight. Antibodies were washed for 15 min three times, then Goat anti-Mouse Alexa Fluor™ Plus 488 antibody (A-11001) and Goat anti-Rabbit Alexa Fluor™ Plus 594 antibody (A-11012) were diluted at 1 : 300 – 1 : 500 ratio by blocking buffer. The cell sample was incubated in the secondary antibody buffer at room temperature for 1h – 3h. Then the cell sample was washed for 15 min three times by 1 × TBST. The cell nuclear was stained by DAPI at 1 : 100 ratio for 30 min and washed. The data was obtained by NIKON A1 HD25 confocal microscope.

Characterization of meiotic oocyte

The ovulated oocyte was fixed by 4% PFA in DPBS with 0.1% Triton-X 100 at 37℃ for 1h. Then oocytes were washed three times by blocking buffer containing 1 × TBST (leagene, PW0020) with 0.3% BSA (Sigma, A1933). Next, oocytes were incubated in blocking buffer with 1 : 50 dilution of anti-α-tubulin (Cell Signaling Technology, 5063S) at 4℃ overnight. The anti-α-tubulin was washed three times by blocking buffer and stained with DAPI of 1 : 100 dilution. The image was obtained by NIKON A1 HD25 confocal microscope.

Histological analysis of folliculogenesis

Follicles within the micro-cavity ovary were fixed by 4% PFA in DPBS for 30 min. Then the scaffold was washed by DPBS twice. 2% Gelatin and 2% agar solution was prepared in water, then the scaffold with follicles was encapsulated by the solution. After gelation, the scaffold was dissociated from the gel, then sequentially dehydrated by gradient ethanol, embedded in paraffin, and sectioned at 5 μm. The section slide was stained with hematoxylin and eosin and visualized by Olympus IX73 microscope.

Hormone ELISAs

Mouse Amh (CUSABIO, CSB-E13156m), estradiol (Cayman, 501890), and Inhibin-A (CUSABIO, CSB-E08238M) and Inhibin-B (CUSABIO, CSB-E08151m) hormones were tested by the corresponding ELISA kit. In brief, the supernatant of the culture medium was collected and diluted in a proper concentration to match the dynamic range of each ELISA kit. Each sample of ELISA was performed in duplicate, as at least three independent experiments. 50 μl of each sample was incubated in the ELISA plate at 37℃ for 1h, then washed three times. The ELISA-based color reaction was performed, and the ELISA plate was read at 450 nm by Thermo Multiskan Skyhigh optical reader to measure the concentration of each sample.

Single-cell RNA-seq pre-processing

GV, SO-MII, and MOC-MII oocytes were obtained, who used Smart-Seq2 protocol to prepare the RNA-seq libraries with a few modifications[65-67]. First, the zona pellucida was removed by Tyrode′s solution (Sigma, T1788). Then, the naked oocyte was digested in 2.55ul cell lysis buffer containing RNase inhibitor (40 U/μL, TaKaRa,

2313A), Triton X-100 solution (10%, Sigma, 9036-19-5), Barcode primer (5 μM), and dNTP mix (10 mM, TaKaRa, 4019). The reverse transcription reaction was performed with 25 nt oligo (dT) primer anchored with an 8 nt cell-specific barcode and 8 nt unique molecular identifiers (UMIs)[68-70]. After the first-strand synthesis, the second-strand cDNAs were synthesized, and the cDNAs were amplified by 10-16 cycles of PCR (95 °C for 3 min, then 4 cycles of: 98 °C for 20 s, 65 °C for 30 s, and 72 °C for 5 min, followed by 10-16 cycles at 98 °C for 20 s, 67 °C for 15 s, and 72 °C for 5 min, with a final cycle at 72 °C for 5 min). The amplified cDNAs of the single cells were then pooled together for the following steps. Biotinylated pre-indexed primers were used to further amplify the PCR (95 °C for 3 min, then 4 cycles of: 98 °C for 20 s, 65 °C for 15s, and 72 °C for 5 min, 4 °C hold). Approximately 300 ng cDNA was sheared to approximately 300 bp by Covaris S2, and the 30 terminals of the cDNA was captured by Dynabeads MyOne Streptavidin C1 beads (Thermo Fisher). We constructed a library based on the enriched cDNA fragments, which were attached to the C1 beads, using KAPA Hyper Prep Kits (KK8505). We used the NEB U-shape adaptor for ligation. Libraries were sequenced to generate 150-bp paired-end reads on an Illumina Novaseq 6000 platform.

Single-cell RNA-seq pre-processing

Raw reads are obtained from well-designed scRNA-seq experiments, quality control (QC) is performed. Low-quality bases (usually at the 3′end), TSO sequences, polyA sequences and adapter sequences was removed at this pre-processing step. The stripped sequences were then aligned to the mouse (Mus musculus) reference genome of mm10 using STAR (version 2.7.9a) (parameters: --soloType CB_UMI_Simple --soloCBmatchWLtype 1MM_multi --soloMultiMappers Unique). Seurat (version 4.0.5)[71] was used to normalize and verify expression level of between samples (parameters: default). Raw expression counts are normalized using ‘NormalizeData’ and ‘ScaleData’.

Region segmentation and visualization.

Two major clusters were determined by ‘FindClusters’ function in Seurat with parameters resolution as 0.6, among which SO-MII and MCO-MII were clustered into the same cluster. UMAP was used to visualize the single-cell analysis results.

Similarity evaluation among groups

We selected 2424 marker genes according to published data[72,73] ，and defined the group gene expression value E_C^g as :

$$E_C^g = \frac{1}{N_C} \sum_{cell\ c\ in\ C} E_c^g$$

where E_c^g represents cell gene expression within one group, and Nc represents numbers of cell in group C. We then calculated the Pearson correlation coefficient and visualized the result in heatmap.

Identification of the differentially expressed genes

Within each group in SO-MII, MCO-MII, and GV, we utilized the 'FindAllMarkers' function in Seurat package with parameters logfc.threshold = 1 and min.pct = 0.25 to identify differentially expressed genes.

We used Resampling methods to test the overlap of differentially expressed genes within one group. In SO-MII or MCO-MIIsamples, we resampled 50X times. In each run, we took 20 cells and divided evenly into two categories C_1 and C_2. We next utilized 'FindAllMarkers' function to accordingly identify the differentially expressed genes of C_1 and GV as well as C_2 and GV, selecting top 1000 upregulated and top 1000 downregulated differentially expressed genes of the two comparisons, marked as G_1 and G_2. We then calculated the number $\mathrm{N_i}$ of overlap genes between G_1 and G_2, and finally obtained the mean overlap value by:

$$\mathrm{N} = \frac{1}{50}\sum_{i=1}^{50} N_i$$

where i represents each run in resampling process.

Pathway enrichment analysis

We utilized 'enrichGO' and 'enrichKEGG' function in clusterProfiler package to analysis pathway enrichment of differentially expressed genes, where parameters were set as pvalueCutoff = 0.05, qvalueCutoff = 0.05. Results were visualized by heatmap, barplot and circos plot.

Putative chromosome ploidy analysis

For CNV analysis, we leverage the R package scCancer developed by Gu Lab[74]. The function 'runMalignancy' was used, while mouse diploid cells were set as reference. Results were visualized by UMAP plot.

Protein networks analysis

The protein networks analysis was performed by STRING online website (Version 11.5) with a cutoff of 0.15.

Acknowledgment

We thank Laboratory Animal Resources Center in Tsinghua University for the support of mice experiments. We thank Jing Zhang at School of Life Sciences in Tsinghua University for contributing to the IVF procedure. We thank for the support of Center of Biomedical Analysis in Tsinghua University. This work was supported by National Key Research and Development Program of China (Grant No. 2018YFA0703004).

Author contributions

M. Y. designed and did most of the experiment. Y. S. did the bioinformatics analysis. B. L., H. L., and Z. W. provided support to the fabrication of micro-cavity ovary. Y. G. and L. O. provided fluorescent gelatin. Z. X. and T. Z. supervised the project. M. Y. wrote the manuscript. J. G., Z. X., and T. Z. revised the manuscript. All authors read and

approved the final manuscript.

Competing interests

The authors declare no competing interests.

Supplementary information

Supplementary figures.
Supplementary tables.
Supplementary movies.

Source data

Confocal images and time-lapse images generated during the study are available for research purposes from the corresponding author on reasonable request. The raw data of single-cell RNA-seq are available in the Genome Sequence Archive (GSA) under accession number CRA007296.

SD fig. 2
Source data for Fig. 2

SD fig. 3
Source data for Fig. 3

SD fig. 5
Source data for Fig. 5

SD fig. S2
Source data for Fig. S2

1 Yoon, J. A., Lee, K. A. & Choi, J. K. A Simplified 3D Culture System for Ovarian Follicles Utilizing a Solid Matrigel Drop to Create an In Vivo-Like Ovarian Microenvironment. *J Biomater Tiss Eng* **9**, 558-561, doi:10.1166/jbt.2019.2018 (2019).

2 Vanacker, J. *et al.* Transplantation of an alginate-matrigel matrix containing isolated ovarian cells: first step in developing a biodegradable scaffold to transplant isolated preantral follicles and ovarian cells. *Biomaterials* **33**, 6079-6085, doi:10.1016/j.biomaterials.2012.05.015 (2012).

3 Vanacker, J. *et al.* Transplantation of an alginate-matrigel matrix containing isolated ovarian cells: First step in developing a biodegradable scaffold to transplant isolated preantral follicles and ovarian cells. *Biomaterials* **33**, 6079-6085, doi:10.1016/j.biomaterials.2012.05.015 (2012).

4 Joo, S. *et al.* The effect of collagen hydrogel on 3D culture of ovarian follicles. *Biomedical Materials* **11**, doi:Artn 065009

10.1088/1748-6041/11/6/065009 (2016).
5 Vanacker, J. & Amorim, C. A. Alginate: A Versatile Biomaterial to Encapsulate Isolated Ovarian Follicles. *Annals of Biomedical Engineering* **45**, 1633-1649, doi:10.1007/s10439-017-1816-6 (2017).
6 Shikanov, A., Xu, M., Woodruff, T. K. & Shea, L. D. Interpenetrating fibrin-alginate matrices for in vitro ovarian follicle development. *Biomaterials* **30**, 5476-5485, doi:10.1016/j.biomaterials.2009.06.054 (2009).
7 Desai, N., Abdelhafez, F., Calabro, A. & Falcone, T. Three dimensional culture of fresh and vitrified mouse pre-antral follicles in a hyaluronan-based hydrogel: a preliminary investigation of a novel biomaterial for in vitro follicle maturation. *Reprod Biol Endocrin* **10**, doi:Artn 29
10.1186/1477-7827-10-29 (2012).
8 Shikanov, A., Smith, R. M., Xu, M., Woodruff, T. K. & Shea, L. D. Hydrogel network design using multifunctional macromers to coordinate tissue maturation in ovarian follicle culture. *Biomaterials* **32**, 2524-2531, doi:10.1016/j.biomaterials.2010.12.027 (2011).
9 Reed, B. G. & Carr, B. R. in *Endotext* (eds K. R. Feingold *et al.*) (2000).
10 Holesh, J. E., Bass, A. N. & Lord, M. in *StatPearls* (2022).
11 Kumar, P. & Sait, S. F. Luteinizing hormone and its dilemma in ovulation induction. *J Hum Reprod Sci* **4**, 2-7, doi:10.4103/0974-1208.82351 (2011).
12 Richards, J. S., Russell, D. L., Robker, R. L., Dajee, M. & Alliston, T. N. Molecular mechanisms of ovulation and luteinization. *Mol Cell Endocrinol* **145**, 47-54, doi:10.1016/s0303-7207(98)00168-3 (1998).
13 Filicori, M. *et al.* The use of LH activity to drive folliculogenesis: exploring uncharted territories in ovulation induction. *Human Reproduction Update* **8**, 543-557, doi:DOI 10.1093/humupd/8.6.543 (2002).
14 Shah, J. S. *et al.* Biomechanics and mechanical signaling in the ovary: a systematic review. *J Assist Reprod Gen* **35**, 1135-1148, doi:10.1007/s10815-018-1180-y (2018).
15 Shikanov, A., Xu, M., Woodruff, T. K. & Shea, L. D. Interpenetrating fibrin-alginate matrices for in vitro ovarian follicle development. *Biomaterials* **30**, 5476-5485, doi:10.1016/j.biomaterials.2009.06.054 (2009).
16 Komatsu, K. & Masubuchi, S. Observation of the dynamics of follicular development in the ovary. *Reproductive Medicine and Biology* **16**, 21-27, doi:10.1002/rmb2.12010 (2017).
17 McKey, J., Cameron, L. A., Lewis, D., Batchvarov, I. S. & Capel, B. Combined iDISCO and CUBIC tissue clearing and lightsheet microscopy for in toto analysis of the adult mouse ovary. *Biology of Reproduction* **102**, 1080-1089, doi:10.1093/biolre/ioaa012 (2020).
18 Zorlutuna, P. *et al.* Microfabricated Biomaterials for Engineering 3D Tissues. *Adv Mater* **24**, 1782-1804, doi:10.1002/adma.201104631 (2012).
19 McGuigan, A. P., Bruzewicz, D. A., Glavan, A., Butte, M. & Whitesides, G. M. Cell Encapsulation in Sub-mm Sized Gel Modules Using Replica Molding. *Plos One* **3**, doi:ARTN e2258
10.1371/journal.pone.0002258 (2008).
20 Du, Y. A., Lo, E., Ali, S. & Khademhosseini, A. Directed assembly of cell-laden microgels for fabrication of 3D tissue constructs. *P Natl Acad Sci USA* **105**, 9522-9527, doi:10.1073/pnas.0801866105 (2008).

21 Bhamare, N., Tardalkar, K., Khadilkar, A., Parulekar, P. & Joshi, M. G. Tissue engineering of human ear pinna. *Cell Tissue Bank*, doi:10.1007/s10561-022-09991-7 (2022).
22 Khademhosseini, A. *et al.* Micromolding of photocrosslinkable hyaluronic acid for cell encapsulation and entrapment. *Journal of Biomedical Materials Research Part A* **79a**, 522-532, doi:10.1002/jbm.a.30821 (2006).
23 Whitesides, G. M. The origins and the future of microfluidics. *Nature* **442**, 368-373, doi:10.1038/nature05058 (2006).
24 Nie, M. H. & Takeuchi, S. Bottom-up biofabrication using microfluidic techniques. *Biofabrication* **10**, doi:ARTN 044103
10.1088/1758-5090/aadef9 (2018).
25 Lin, D. G. *et al.* Microgel Single-Cell Culture Arrays on a Microfluidic Chip for Selective Expansion and Recovery of Colorectal Cancer Stem Cells. *Analytical Chemistry* **93**, 12628-12638, doi:10.1021/acs.analchem.1c02335 (2021).
26 Alonso, D. G., Yu, M. C., Qu, H. J., Ma, L. & Shen, F. Advances in Microfluidics-Based Technologies for Single Cell Culture. *Adv Biosyst* **3**, doi:ARTN 1900003
10.1002/adbi.201900003 (2019).
27 Lin, R. Z., Chen, Y. C., Moreno-Luna, R., Khademhosseini, A. & Melero-Martin, J. M. Transdermal regulation of vascular network bioengineering using a photopolymerizable methacrylated gelatin hydrogel. *Biomaterials* **34**, 6785-6796, doi:10.1016/j.biomaterials.2013.05.060 (2013).
28 Kim, P., Yuan, A., Nam, K. H., Jiao, A. & Kim, D. H. Fabrication of poly(ethylene glycol): gelatin methacrylate composite nanostructures with tunable stiffness and degradation for vascular tissue engineering. *Biofabrication* **6**, doi:Artn 024112
10.1088/1758-5082/6/2/024112 (2014).
29 Shin, S. R. *et al.* Reduced Graphene Oxide-GelMA Hybrid Hydrogels as Scaffolds for Cardiac Tissue Engineering. *Small* **12**, 3677-3689, doi:10.1002/smll.201600178 (2016).
30 Qi, H. *et al.* Patterned Differentiation of Individual Embryoid Bodies in Spatially Organized 3D Hybrid Microgels. *Adv Mater* **22**, 5276-5281, doi:10.1002/adma.201002873 (2010).
31 Saatcioglu, H. D., Cuevas, I. & Castrillon, D. H. Control of Oocyte Reawakening by Kit. *Plos Genet* **12**, doi:ARTN e1006215
10.1371/journal.pgen.1006215 (2016).
32 Griffin, J., Emery, B. R., Huang, I., Peterson, C. M. & Carrell, D. T. Comparative analysis of follicle morphology and oocyte diameter in four mammalian species (mouse, hamster, pig, and human). *J Exp Clin Assist Reprod* **3**, 2, doi:10.1186/1743-1050-3-2 (2006).
33 Grynnerup, A. G., Lindhard, A. & Sorensen, S. The role of anti-Mullerian hormone in female fertility and infertility - an overview. *Acta Obstet Gynecol Scand* **91**, 1252-1260, doi:10.1111/j.1600-0412.2012.01471.x (2012).
34 Brook, M., Smith, J. W. & Gray, N. K. The DAZL and PABP families: RNA-binding proteins with interrelated roles in translational control in oocytes. *Reproduction* **137**, 595-617, doi:10.1530/REP-08-0524 (2009).
35 Nardone, G. *et al.* YAP regulates cell mechanics by controlling focal adhesion assembly. *Nat Commun* **8**, 15321, doi:10.1038/ncomms15321 (2017).
36 Geuens, T., van Blitterswijk, C. A. & LaPointe, V. L. S. Overcoming kidney organoid challenges for regenerative medicine. *Npj Regen Med* **5**, doi:ARTN 8

10.1038/s41536-020-0093-4 (2020).
37 Peired, A. J. *et al.* Bioengineering strategies for nephrologists: kidney was not built in a day. *Expert Opin Biol Ther* **20**, 467-480, doi:10.1080/14712598.2020.1709439 (2020).
38 Lewis-Israeli, Y. R. *et al.* Self-assembling human heart organoids for the modeling of cardiac development and congenital heart disease. *Nature Communications* **12**, doi:ARTN 5142
10.1038/s41467-021-25329-5 (2021).
39 Drakhlis, L. *et al.* Human heart-forming organoids recapitulate early heart and foregut development. *Nat Biotechnol* **39**, 737-746, doi:10.1038/s41587-021-00815-9 (2021).
40 Nugraha, B., Buono, M. F., von Boehmer, L., Hoerstrup, S. P. & Emmert, M. Y. Human Cardiac Organoids for Disease Modeling. *Clin Pharmacol Ther* **105**, 79-85, doi:10.1002/cpt.1286 (2019).
41 Lewis-Israeli, Y. R., Wasserman, A. H. & Aguirre, A. Heart Organoids and Engineered Heart Tissues: Novel Tools for Modeling Human Cardiac Biology and Disease. *Biomolecules* **11**, doi:ARTN 1277
10.3390/biom11091277 (2021).
42 Lee, J. *et al.* In vitro generation of functional murine heart organoids via FGF4 and extracellular matrix. *Nature Communications* **11**, doi:ARTN 4283
10.1038/s41467-020-18031-5 (2020).
43 Goldfracht, I. *et al.* Generating ring-shaped engineered heart tissues from ventricular and atrial human pluripotent stem cell-derived cardiomyocytes. *Nature Communications* **11**, doi:ARTN 75
10.1038/s41467-019-13868-x (2020).
44 Zimmermann, W. H., Melnychenko, I. & Eschenhagen, T. Engineered heart tissue for regeneration of diseased hearts. *Biomaterials* **25**, 1639-1647, doi:10.1016/S0142-9612(03)00521-0 (2004).
45 Goldfracht, I. *et al.* Engineered heart tissue models from hiPSC-derived cardiomyocytes and cardiac ECM for disease modeling and drug testing applications. *Acta Biomaterialia* **92**, 145-159, doi:10.1016/j.actbio.2019.05.016 (2019).
46 Mannhardt, I. *et al.* Human Engineered Heart Tissue: Analysis of Contractile Force. *Stem Cell Reports* **7**, 29-42, doi:10.1016/j.stemcr.2016.04.011 (2016).
47 O'Neill, J. D., Pinezich, M. R., Guenthart, B. A. & Vunjak-Novakovic, G. Gut bioengineering strategies for regenerative medicine. *Am J Physiol Gastrointest Liver Physiol* **320**, G1-G11, doi:10.1152/ajpgi.00206.2020 (2021).
48 Kozlowski, M. T., Crook, C. J. & Ku, H. T. Towards organoid culture without Matrigel. *Commun Biol* **4**, doi:ARTN 1387
10.1038/s42003-021-02910-8 (2021).
49 Cai, L. J. *et al.* Anisotropic Microparticles from Microfluidics. *Chem-Us* **7**, 93-136, doi:10.1016/j.chempr.2020.09.023 (2021).
50 Laronda, M. M. *et al.* A bioprosthetic ovary created using 3D printed microporous scaffolds restores ovarian function in sterilized mice. *Nature Communications* **8**, doi:ARTN 15261
10.1038/ncomms15261 (2017).
51 Wu, T. *et al.* Three-dimensional bioprinting of artificial ovaries by an extrusion-based

method using gelatin-methacryloyl bioink. *Climacteric*, doi:10.1080/13697137.2021.1921726 (2021).

52 Zubizarreta, M. E. & Xiao, S. Bioengineering models of female reproduction. *Bio-Des Manuf* **3**, 237-251, doi:10.1007/s42242-020-00082-8 (2020).

53 MacLennan, M., Crichton, J. H., Playfoot, C. J. & Adams, I. R. Oocyte development, meiosis and aneuploidy. *Semin Cell Dev Biol* **45**, 68-76, doi:10.1016/j.semcdb.2015.10.005 (2015).

54 Merrick, W. C. & Pavitt, G. D. Protein Synthesis Initiation in Eukaryotic Cells. *Cold Spring Harb Perspect Biol* **10**, doi:10.1101/cshperspect.a033092 (2018).

55 Dever, T. E., Dinman, J. D. & Green, R. Translation Elongation and Recoding in Eukaryotes. *Cold Spring Harb Perspect Biol* **10**, doi:10.1101/cshperspect.a032649 (2018).

56 Arroyo, A., Kim, B. & Yeh, J. Luteinizing Hormone Action in Human Oocyte Maturation and Quality: Signaling Pathways, Regulation, and Clinical Impact. *Reprod Sci* **27**, 1223-1252, doi:10.1007/s43032-019-00137-x (2020).

57 Jeong, S. I. *et al.* XAF1 forms a positive feedback loop with IRF-1 to drive apoptotic stress response and suppress tumorigenesis. *Cell Death Dis* **9**, 806, doi:10.1038/s41419-018-0867-4 (2018).

58 Zhu, L. M. *et al.* Tumor suppressor XAF1 induces apoptosis, inhibits angiogenesis and inhibits tumor growth in hepatocellular carcinoma. *Oncotarget* **5**, 5403-5415, doi:10.18632/oncotarget.2114 (2014).

59 Fong, W. G. *et al.* Expression and genetic analysis of XIAP-associated factor 1 (XAF1) in cancer cell lines. *Genomics* **70**, 113-122, doi:10.1006/geno.2000.6364 (2000).

60 Liu, J. *et al.* [Effect of stable overexpression of XAF1 gene on biological characteristics of ovarian cancer A2780 cells]. *Nan Fang Yi Ke Da Xue Xue Bao* **41**, 760-766, doi:10.12122/j.issn.1673-4254.2021.05.18 (2021).

61 Dupont, S. Role of YAP/TAZ in cell-matrix adhesion-mediated signalling and mechanotransduction. *Exp Cell Res* **343**, 42-53, doi:10.1016/j.yexcr.2015.10.034 (2016).

62 Zou, R. *et al.* YAP nuclear-cytoplasmic translocation is regulated by mechanical signaling, protein modification, and metabolism. *Cell Biology International* **44**, 1416-1425, doi:10.1002/cbin.11345 (2020).

63 Tang, Y., Wang, W., Ni, L. & Liu, H. C. A Modified Protocol for in Vitro Maturation of Mouse Oocytes from Secondary Preantral Follicles. *Fertility and Sterility* **96**, S241-S241, doi:DOI 10.1016/j.fertnstert.2011.07.924 (2011).

64 Belli, M. *et al.* Towards a 3D culture of mouse ovarian follicles. *International Journal of Developmental Biology* **56**, 931-937, doi:10.1387/ijdb.120175mz (2012).

65 Kannanayakal, T. J. & Eberwine, J. mRNA methods used in dissecting gene expression of the brain. *Ageing Res Rev* **4**, 513-528, doi:10.1016/j.arr.2005.09.001 (2005).

66 Picelli, S. *et al.* Smart-seq2 for sensitive full-length transcriptome profiling in single cells. *Nat Methods* **10**, 1096-1098, doi:10.1038/nmeth.2639 (2013).

67 Spaethling, J. M. *et al.* Single-cell transcriptomics and functional target validation of brown adipocytes show their complex roles in metabolic homeostasis. *Faseb J* **30**, 81-92, doi:10.1096/fj.15-273797 (2016).

68 Hashimshony, T., Wagner, F., Sher, N. & Yanai, I. CEL-Seq: single-cell RNA-Seq by multiplexed linear amplification. *Cell Rep* **2**, 666-673, doi:10.1016/j.celrep.2012.08.003 (2012).

69 Islam, S. *et al.* Highly multiplexed and strand-specific single-cell RNA 5' end sequencing. *Nat Protoc* **7**, 813-828, doi:10.1038/nprot.2012.022 (2012).
70 Klein, A. M. *et al.* Droplet barcoding for single-cell transcriptomics applied to embryonic stem cells. *Cell* **161**, 1187-1201, doi:10.1016/j.cell.2015.04.044 (2015).
71 Stuart, T. *et al.* Comprehensive Integration of Single-Cell Data. *Cell* **177**, 1888-+, doi:10.1016/j.cell.2019.05.031 (2019).
72 Cui, X. S. *et al.* Maternal gene transcription in mouse oocytes: Genes implicated in oocyte maturation and fertilization. *J Reprod Develop* **53**, 405-418, doi:DOI 10.1262/jrd.18113 (2007).
73 Zhao, Z. H. *et al.* RNA-Seq transcriptome reveals different molecular responses during human and mouse oocyte maturation and fertilization. *Bmc Genomics* **21**, doi:ARTN 475 10.1186/s12864-020-06885-4 (2020).
74 Guo, W. *et al.* scCancer: a package for automated processing of single-cell RNA-seq data in cancer. *Brief Bioinform* **22**, doi:10.1093/bib/bbaa127 (2021).

Supplementary Files

This is a list of supplementary files associated with this preprint. Click to download.

- supplementaryfigures.pdf
- movieS1.mp4
- movieS2.mp4
- S1GVvsSOMIItop1000.csv
- S2GVvsMCOMIItop1000.csv
- S3Top1000DEGsofSOMIIvsGVUpregulateGO.csv
- S4Top1000DEGsofSOMIIvsGVDownregulateGO.csv
- S5Top1000DEGsofMCOMIIvsGVUpregulateGO.csv
- S6Top1000DEGsofOLMvsGVDownregulateGO.csv